communications biology

Article

https://doi.org/10.1038/s42003-024-06874-3

Cpt1a Drives primed-to-naïve pluripotency transition through lipid remodeling

Zhaoyi Ma[1,2,9], Xingnan Huang[2,9], Junqi Kuang[2,3,4], Qiannan Wang[2], Yue Qin[2,3,4], Tao Huang[1,2], Zechuan Liang[1,2], Wei Li[5,6], Yu Fu[2], Pengli Li[5,6], Yixin Fan[5,6], Ziwei Zhai[5,6], Xiaomin Wang[2], Jin Ming[2,3], Chengchen Zhao[2,4,7], Bo Wang[2,7,8] & Duanqing Pei[2,4]

Metabolism has been implicated in cell fate determination, particularly through epigenetic modifications. Similarly, lipid remodeling also plays a role in regulating cell fate. Here, we present comprehensive lipidomics analysis during BMP4-driven primed to naive pluripotency transition or BiPNT and demonstrate that lipid remodeling plays an essential role. We further identify *Cpt1a* as a rate-limiting factor in BiPNT, driving lipid remodeling and metabolic reprogramming while simultaneously increasing intracellular acetyl-CoA levels and enhancing H3K27ac at chromatin open sites. Perturbation of BiPNT by histone acetylation inhibitors suppresses lipid remodeling and pluripotency transition. Together, our study suggests that lipid remodeling promotes pluripotency transitions and further regulates cell fate decisions, implicating *Cpt1a* as a critical regulator between primed-naive cell fate control.

Metabolism plays a pivotal role in cell fate decisions[1–4]. Yet, how metabolism enables cell fate transition remains less well understood mechanistically. Recent advances in tools such as LC-MS and ChIP-seq are transforming our understanding of metabolomic impact on epigenetic changes[5–10]. Thus, by combining metabolomics and epigenomics analyses may open new avenues in our understanding of cell fate control. Accumulating evidence suggests that metabolic changes may modulate processes involving both epigenetics and cell signaling pathways that lead to cell fate transition[5,6,9–12]. Lipids, as essential cellular components and nutrients, participate in regulating cell fate in various ways[13–16]. Embryonic development before and after implantation exhibits distinct lipid metabolic profiles[17–19]. Given the difficulty of accessing this developmental "black box" period[20,21], it is essential to simulate these stages in vitro to study lipid remodeling.

Mouse embryonic stem cells (ESCs) and epiblast stem cells (EpiSCs) are derived from pre- and post-implantation stages of the embryo, respectively, and represent two distinct states of pluripotency: naive and primed[22,23]. These states exhibit marked differences in morphology, gene expression, maintenance conditions, epigenetic status, and metabolic profiles, impaction of chimeric competence[20,24–27]. Metabolically, ESCs predominantly rely on oxidative phosphorylation and lipolysis, while EpiSCs favor glycolysis for energy production and enhanced lipid synthesis[5,13,28–30]. ESCs can differentiate into states akin to EpiSCs, and EpiSCs can revert to states resembling naïve ESCs[25,26,31–34]. This transition involves metabolic reprogramming from naïve to primed states and vice versa[5,17,28,30]. However, the lipid metabolic profile during the pluripotency transition in the PNT process has not yet been delineated, and the specific role of lipid remodeling remains unclear.

We have recently developed a BMP4-induced system (BiPNT) that facilitates the primed to naïve transition, with ~80% efficiencies[33,34]. This system may serve as an ideal model to investigate how lipid metabolism influences cell fate control. To this end, we report that *Cpt1a*, a key enzyme in lipid metabolism, significantly impacts the transition from primed to naïve states by facilitating lipid remodeling and metabolic reprogramming and by increasing cellular acetyl-CoA levels and histone acetylation. Our results suggest that lipid remodeling is crucial for the process of pluripotent transition and can regulate cell fate decisions.

[1]College of Life Sciences, Zhejiang University, Hangzhou, China. [2]Laboratory of Cell Fate Control, School of Life Sciences, Westlake University, Hangzhou, China. [3]Institute of Biology, Westlake Institute for Advanced Study, Hangzhou, China. [4]Westlake Laboratory of Life Sciences and Biomedicine, Hangzhou, Zhejiang, China. [5]Laboratory on Stem Cell and Regenerative Medicine, Guangzhou Institutes of Biomedicine and Health, Chinese Academy of Sciences, Guangzhou, China. [6]University of Chinese Academy of Sciences, Beijing, China. [7]Zhejiang Key Laboratory of Biomedical Intelligent Computing Technology, Hangzhou, China. [8]Zhejiang University of Science and Technology School of Information and Electronic Engineering, Hangzhou, China. [9]These authors contributed equally: Zhaoyi Ma, Xingnan Huang. e-mail: peiduanqing@westlake.edu.cn

Results

Metabolic switch during PNT

A pronounced metabolic switch has been reported between preimplantation to postimplantation embryos and reflected in the naive and primed states of mouse embryonic stem cells[5,28,30]. To probe the molecular mechanism associated with this switch, we performed transcriptomic and metabolomic profilings on primed and naive stem cells[33,34]. Gene Ontology (GO) analyses confirm that the primed EpiSCs are highly glycolytic, whereas the naive ESCs with robust lipid metabolism and fatty acid oxidation (Supplementary Fig. 1a). Further metabolomics analysis reveals significant differences between these two pluripotent states (Supplementary Fig. 1b, 1c).

To identify critical drivers for this robust metabolic reprogramming during the pluripotency transition, we used a robust BMP4 induced primed-to-naïve transition (BiPNT) system established in our lab[33,34], which can convert ~80% EpiSCs to chimera-competent naïve colonies (Supplementary Fig. 1d). We performed transcriptomics, metabolomics, and lipidomics during PNT at D0 (EpiSCs), D3, D5, and D8 cells and reset naive state stem cells (rESCs) (Fig. 1a). Principal component analyses (PCA) of transcriptomics, metabolomics, and lipidomics show interesting patterns of dynamic switches mirroring each other (Fig. 1b and Supplementary Fig. 1e-g).

We then focused on ~3000 metabolism-related genes, including enzymes and transporters[35]. We show that these genes are categorized into five clusters using *k*-means clustering, and distinct stage-specific expression patterns (Fig. 1c)[9]. KEGG pathway enrichment analysis of RNA-seq data revealed that glycolysis, pyruvate metabolism, and fatty acid biosynthesis-related genes were enriched in the D0 (EpiSCs state) gene cluster, and various lipid metabolism-related genes were enriched in the D3, D5, and D8 clusters, and oxidative phosphorylation (OxPhos), TCA cycle, and fatty acid degradation-related genes were enriched in rESCs (Fig. 1d). Interestingly, both transcriptomics and lipidomics analyses unveiled that lipid metabolism is activated in the PNT process, especially on D3, D5, and D8 (Fig. 1e and Supplementary Fig. 1g). These results suggest that activation of lipid metabolism during the intermediate states may drive the PNT Process.

Lipid remodeling during PNT

To explore the mechanism associated with lipid remodeling during PNT, we correlated lipid species with the expression of lipid metabolism-related genes[36] and showed that lipids and associated genes could be classified into six distinct clusters, i.e., G1-6 (Figs. 1e, f and Supplementary Figs. 2 and 3). We then characterized the mean expression changes of six clusters of genes in the PNT process. We show that G1, G2, and G3 are mainly actively expressed in the PNT process. In contrast, genes in G4 show a monotonically increasing expression trend. G5 shows a reverse trend, characterized by a monotonically decreasing pattern. However, G6 exhibits active expression in both EpiSCs and rESCs and shows a reduction in expression during the PNT process (Fig. 1f). GO enrichment analysis also shows that G1, G2, G3, and G6 are mainly enriched in various lipid metabolisms, especially phospholipid metabolism. G4 and G5 are enriched in lipid degradation metabolism and lipid synthesis metabolism, respectively (Supplementary Fig. 2). This phenomenon is consistent with previously reported lipid utilization patterns in primed and naïve cells[5,17,18].

We further enriched lipid species and saturation for each lipid cluster[14]. It reveals that glycerophospholipids, such as PC and PE, predominantly accumulate in L2 and L4, while glycerides, like TG and DG, are concentrated in L1 and L6 (Fig. 1g and Supplementary Fig. 3a, b). Subsequently, we quantified the distribution of differentially abundant lipid species in lipid clusters relative to EpiSCs samples[36]. We clearly observed significant compositional shifts in various differential lipids in the PNT process (Fig. 1h and Supplementary Fig. 3c). Collectively, these results again strongly suggest that lipid remodeling may drive PNT.

Cpt1a contributes to BiPNT

To identify genes involved in lipid remodeling that may drive PNT, we focused on Gene cluster 4 (G4) (Fig. 1f). We found significant upregulation of genes like *Cpt1a*, *Inpp5d*, *Itpka*, and *Lima1* in rESCs, compared to EpiSCs (Fig. 2a). GO enrichment analysis of upregulated genes largely pointed to pathways related to fatty acid and TG metabolism, lipid catabolism, and acetyl-CoA metabolism in rESCs, with fatty acid metabolism being the most prominent (Fig. 2b). Notably, the heatmap of fatty acid metabolic genes in the PNT process indicates a progressive increase (Fig. 2c). *Cpt1a* is the rate-limiting enzyme in transporting activated medium and long-chain fatty acids into mitochondria for β-oxidation, and its expression level directly impacts FAO levels[29,37–39]. During embryonic development from E3.5 to E6.5, there is a noticeable decline in the expression of *Cpt1a*[40]. Conversely, the steady increase of *Cpt1a* was observed in the Primed to Naïve transition (Fig. 2d, Supplementary Fig. 4a).

Initially, we used Etomoxir (ETO), a common CPT1A inhibitor, to treat in stage 1 of the BiPNT process, significantly reducing GFP-positive clones (Supplementary Fig. 4b). To evaluate *Cpt1a* function, we overexpressed it in EpiSCs, observing no significant impact on cell morphology or proliferation and maintaining sub-cellular localization consistent with the endogenous protein (Supplementary Fig. 4d–f). We used the BiPNT system[33,34], these cells (*Cpt1a-OE*) and empty vector-treated (Control) EpiSCs were induced into a naïve state. Remarkably, overexpression of *Cpt1a* significantly enhanced PNT induction efficiency, achieving a 95% success rate (Fig. 2e–g and Supplementary Fig. 4c). Timecourse analysis revealed a positivity rate nearly double that of Control by Day 6 (Figs. 2h, i), with similar trends in GFP clone counts (Supplementary Fig. 4h). However, in the absence of BMP4, routine PNT induction was not achievable (Supplementary Fig. 4m). Combining this with our previous RNA-seq data analysis[33], we also discovered that *Cpt1a* expression is extremely low in the induction system without BMP4, showing significant differences from the normal system. This suggests that the activation of *Cpt1a* may be dependent on pathways related to BMP4, necessitating further research to investigate its activation and regulatory molecular mechanisms. Together, these results suggest that overexpression of *Cpt1a* might accelerate the BiPNT process.

Critically, both knocking down and knocking out *Cpt1a* significantly reduced GFP clone numbers. Overexpression partially rescued the knockout phenotype (Fig. 2j and Supplementary Fig. 4j). Crucially, irrespective of whether *Cpt1a* was overexpressed or knocked out, the successfully induced rESCs were able to maintain a normal naïve state, suggesting that *Cpt1a* is not indispensable for maintaining pluripotency (Fig. 2k and Supplementary Fig. 4g, 4i–l). These results demonstrate that *Cpt1a* contributes to BiPNT.

Cpt1a drives lipid remodeling and metabolic reprogramming during PNT

To uncover the molecular mechanism of *Cpt1a* in the BiPNT process[33,34], we conducted a multi-omics analysis incorporating transcriptomics, lipidomics and polar metabolomics, proteomics, and epigenomics between Control and *Cpt1a-OE* (OE) samples on day 3 (Fig. 3a). We performed correlation analyses between differential transcriptomics and lipidomics profiles[36]. RNA-seq analysis highlighted alterations in over 100 lipid metabolism genes between Control and OE groups, indicating heightened metabolic activation (Fig. 3b and Supplementary Fig. 5a, b), linked to various lipid metabolism classes.

Aligning with observed impacts on lipid metabolic genes in *Cpt1a-OE*, lipidomics analysis demonstrated lipid remodeling upon *Cpt1a* overexpression. We compared lipidomics differences between conditions, with PCA and volcano plots distinctly showing significant disparities (Fig. 3c, d). Remarkably, Gene-set enrichment analysis (GSEA) revealed a concurrent upregulation trend of pluripotency genes and lipid metabolism in OE conditions (Fig. 3e). To further explore lipid remodeling, consistent with prior lipid-gene association analyses, we noted increasing proportions of L2 and L3 lipids and reduced quantities of L1, L5, and L6 lipids in OE condition (Fig. 3f). Significantly, lipid category ratio analysis under OE conditions showed an increase in glycerophospholipids and a reduction of glycerides (Fig. 3g). Detailed analysis of lipid classes and their abundance showed a notable increase in PE, PC, PG and a decrease in TG and DG (Fig. 3h–k, Supplementary Fig. 5c–e). It suggests that enhanced glyceride consumption

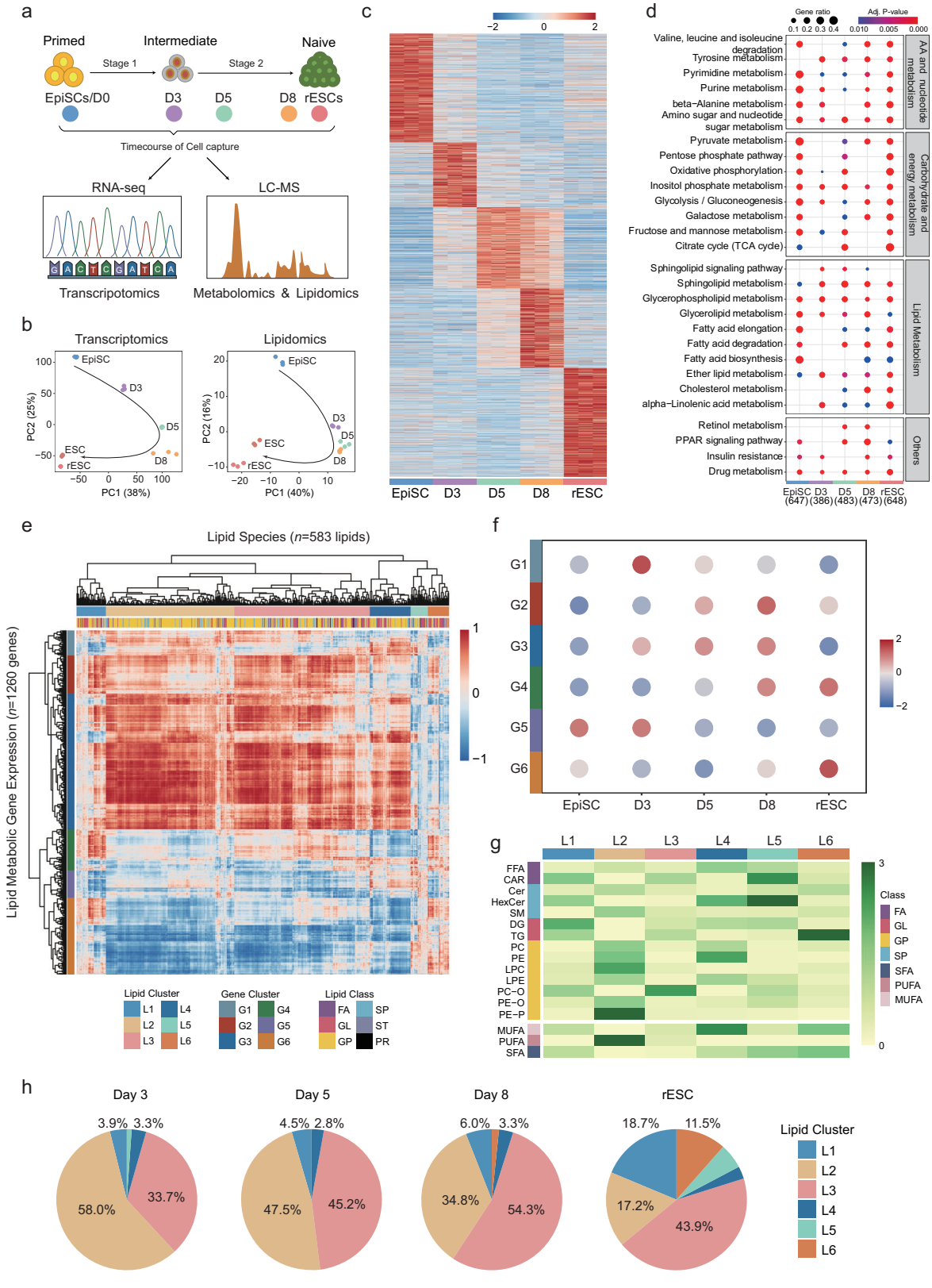

leads to higher production of functional lipids like glycerophospholipids in OE conditions, thereby driving lipid remodeling. These data suggest a role for lipid remodeling in pluripotency regulation.

We also examined the transcriptome and lipidome under *Cpt1a* deletion (KO) conditions, observing a marked downregulation of lipid metabolism genes and inhibiting fatty acid oxidation (Supplementary Fig. 6a, b). GSEA analysis indicated a concurrent downregulation of lipid metabolism and pluripotency genes in KO conditions (comparison with WT) (Supplementary Fig. 6c), contrasting with OE conditions (comparison with Control) (Fig. 3e). GO enrichment showed similar trends (Supplementary Fig. 6d). Notably, the activation of apoptosis-related pathways is consistent with our observations of increased cell death during intermediate stages of PNT

Fig. 1 | Integrative analysis of transcriptomics and lipidomics reveals lipid remodeling in Primed-to-Naive pluripotency transition. a Schematic overview for transcriptomics, metabolomics, and lipidomics profiling of BMP4 induced Primed-Naïve Transition (BiPNT). LC-MS, Liquid Chromatography Mass Spectrometry. **b** Principal component analysis of transcriptomics and lipidomics showed the lipid remodeling during the PNT process. **c** *k*-means clustering classified approximately 3000 metabolism-associated genes into five clusters. Each cluster corresponding to a distinct timepoint. Distinct colors represent corresponding timepoints. **d** KEGG pathway analysis of the five stage-specific metabolic gene clusters from **c.** **e** Correlation matrix visualizing coordination of lipid species and lipid-related genes. Lipid species ($n = 1260$ genes) correlate with lipid metabolism genes throughout PNT. Difference colors represent distinct lipid clusters, gene clusters, and lipid classes. **f** Bubble plot depicting mean expression of each gene cluster in PNT. Different gene clusters were annotated using the corresponding colors indicated in **e**. **g** Lipid class and saturation enrichment for six lipid clusters (significance calculated by a hypergeometric test against total lipidome with false discovery rate adjustment). Different lipid clusters and lipid classes were annotated using the corresponding colors found in **e**. **h** Pie charts representing the distribution of over-enriched lipid clusters for differentially abundant lipid species in altered samples relative to EpiSC (D0) samples. FA Fatty acids, GL glycerolipids, GP glycerophospholipids, SP sphingolipids, ST sterol lipids, PR prenol lipids. CAR Acly carnitines, Cer ceramide, DG diacylglycerol, FFA free fatty acid, HexCer hexosylceramide, LPE lysophosphatidylcholine, LPC lysophosphatidylethanolamine, PC phosphatidylcholine, PC-O alkyl-ether-linked phosphatidylcholine, PE phosphatidylethanolamine, PE-O alkyl-ether-linked phosphatidylethanolamine, PE-P vinyl-ether-linked phosphatidylethanolamine, SM sphingomyelin, TG triacylglyceride. MUFA monounsaturated fatty acids, PUFA polyunsaturated fatty acids, SFA saturated fatty acids. Source data are provided as Supplementary Data 1.

induction in KO cell lines (Supplementary Fig. 6d), which impedes effective PNT transformation. Lipidomics analysis further revealed the impact of *Cpt1a* KO on lipid metabolism and composition (Supplementary Fig. 6e–i). We speculate that *Cpt1a* deficiency might cause improper lipid remodeling and metabolic switching, which could fail to support the energy and material demands required for cell fate transition, ultimately leading to cell death[29,41–43]. Considering the crucial role of *Cpt1a* in PNT, we subsequently focused our investigations on its impact under OE conditions.

Given the impact of *Cpt1a* on mitochondrial function and metabolic levels[37,39,44–46], we also measured the polar metabolome. The heatmap showed metabolic reprogramming between Control and OE conditions (Fig. 4a). Regarding mitochondrial morphology[45,47,48], both Control and OE conditions exhibited a short, rounded shape (Figs. 4b, c), similar to the naive cell reported previously. Oxygen consumption rate (OCR) measurements revealed higher OCR in OE conditions than in Control on Day 3 (Fig. 4d), indicating enhanced mitochondrial function and increased metabolism. Integrative metabolomic and transcriptomic analyses under OE conditions demonstrated markedly enhanced activity in amino acid metabolism, nucleotide metabolism, CoA synthesis, and lipid metabolism (Fig. 4e). Gene heatmap showed that overexpression of *Cpt1a* primarily impacts fatty acid oxidation, triglyceride, phospholipid, and acetyl-CoA metabolism pathways (Fig. 4f). Combining metabolomic and transcriptomic data, and considering mitochondrial function, we focused on key intermediary metabolites and the cellular regulatory molecular, acetyl-CoA, involved in metabolic remodeling[49–52]. We quantified acetyl-CoA levels using LC-MS. The results showed significantly higher acetyl-CoA in OE conditions, aligning with GSEA analysis of acetyl-CoA metabolism (Figs. 4g, h). These results showed metabolic reprogramming and improved mitochondrial function in OE conditions, suggesting that acetyl-CoA may affect *Cpt1a*-dependent PNT through lipid remodeling and further metabolic reprogramming.

Cpt1a promotes PNT by facilitating histone acetylation

Acetyl-CoA, a key substrate for acetylation, participates in histone modifications[52–54]. To begin to understand the impact of acetyl-CoA on PNT, we first assessed intracellular acetylated peptide modifications. Indeed, overexpression of *Cpt1a* significantly increased intracellular acetylation, predominantly N-acetylation, relative to Control (Supplementary Fig. 7a). Immunofluorescence revealed heightened lysine acetylation in OE conditions (Supplementary Fig. 7b, c). Histone acetylation is a crucial epigenetic mechanism that regulates gene expression by altering chromatin structure, thereby influencing various cell fates[8,10,49,55]. H3K27, a common acetylation site, serves as an indicator of chromatin openness and is often analyzed alongside ACAT-seq data to assess chromatin accessibility and transcriptional activity[56–58]. Considering the role of H3K27ac in pluripotency gene regulation, we employed CUT&Tag technology to assess H3K27ac levels[59,60].

CUT&Tag analysis indicated elevated global H3K27ac signals in the *Cpt1a-OE* group compared to Control (Fig. 5a and Supplementary Fig. 7d–f). H3K27ac modifications were categorized into three types: unique to Control, common to both, and increase in the OE condition (Fig. 5b). The *Cpt1a-OE* group exhibited increased acetylation in promoters and exons, while Control showed more in intergenic and intron regions (Fig. 5c). Indeed, more than 75% of the H3K27ac-binding sites were genomic regions around the TSSs or more than 10 kb distal to the TSSs, especially in OE conditions (Fig. 5d). Notably, OE conditions showed significant H3K27ac enrichment in enhancers and promoters of lipid metabolism and pluripotency-related genes (Fig. 5e). Cross-referencing 13,471 OE-specific genes regulated by H3K27ac with RNA-seq data identified 384 upregulated genes, including 53 transcription factors (TFs), which encompasses pluripotency markers such as *Sox2*, *Nanog*, *Esrrb*, *Prdm14*, *Klf2*, *Tfap2c*, and lipid metabolic TFs such as *Pparg*, *Cebpa* (Fig. 5f). qPCR analysis demonstrated a consistent trend of upregulation (Fig. 5g). GO enrichment analysis of these genes underscored pathways integral to cell fate, pluripotency, and lipid metabolism (Fig. 5h). In the KO model, we identified 1,210 genes that were concurrently downregulated at both the H3K27ac level across 23,630 sites and in RNA-seq analysis of 1,394 genes (Supplementary Fig. 7g). These genes exhibited decreased H3K27ac levels, notably affecting pluripotency and lipid metabolism pathways (Supplementary Fig. 7h). Further analysis demonstrated that these downregulated genes are primarily involved in pathways regulating cellular pluripotency, cell proliferation, and embryonic development (Supplementary Fig. 7i). These results further elucidate, from an epigenomic and transcriptomic perspective, the occurrence of lethality and apoptosis in the KO experiments, and provide partial evidence of chromatin openness and epigenetic modifications that support previous reports on the impact of *Cpt1a* deficiency on cell survival or developmental potential[29,39,42]. These data suggest that *Cpt1a* expression enhances H3K27ac levels, thereby promoting pluripotency transitions and lipid remodeling.

To verify the impact of histone acetylation on lipid remodeling and pluripotency, we utilized A-485, a histone acetyltransferases (HATs) inhibitor and competitive acetyl-CoA antagonist known for specifically inhibiting H3K18 and H3K27 acetylation[52,61,62]. A-485 (1 μM) treatment was performed on day 2 of stage 1, followed by evaluation of expression changes on day 3 and PNT efficiency on day 8 (Fig. 6a and Supplementary Fig. 8a, b). A-485 significantly reduced GFP clones as expected (Figs. 6b, c). Concurrently, we employed the CBP/P300 inhibitor C646[63] and malonyl-CoA[45], the endogenous allosteric inhibitor of *Cpt1a*, for treatments on day 3, observing phenotypes similar to those treated with A-485. Subsequent analyses of transcriptomic and epigenomic data under A-485 treatment were conducted (Supplementary Fig. 8c, d). To elucidate the regulatory mechanisms of histone modifications, we integrated previously reported ACAT data[33] with our current Cut&Tag data to analyze H3K27ac levels at chromatin open sites on Day 3. OE conditions significantly increased H3K27ac enrichment, whereas A-485 treatment markedly reduced these levels (Fig. 6d). Additionally, genes downregulated in RNA-seq data post A-485 treatment exhibited significant reductions in H3K27ac levels (Fig. 6e). Notably, A-485 effectively countered the upregulation of *Cpt1a*-induced genes, primarily involved in pluripotency and lipid metabolism regulation (Fig. 6f). RNA-seq analysis showed substantial inhibition of lipid gene expression in *Cpt1a-OE* cells by A-485 (Supplementary Fig. 8e). Further GO enrichment and GSEA analyses indicated that A-485 suppresses lipid-related pathways and promotes lineage differentiation under OE

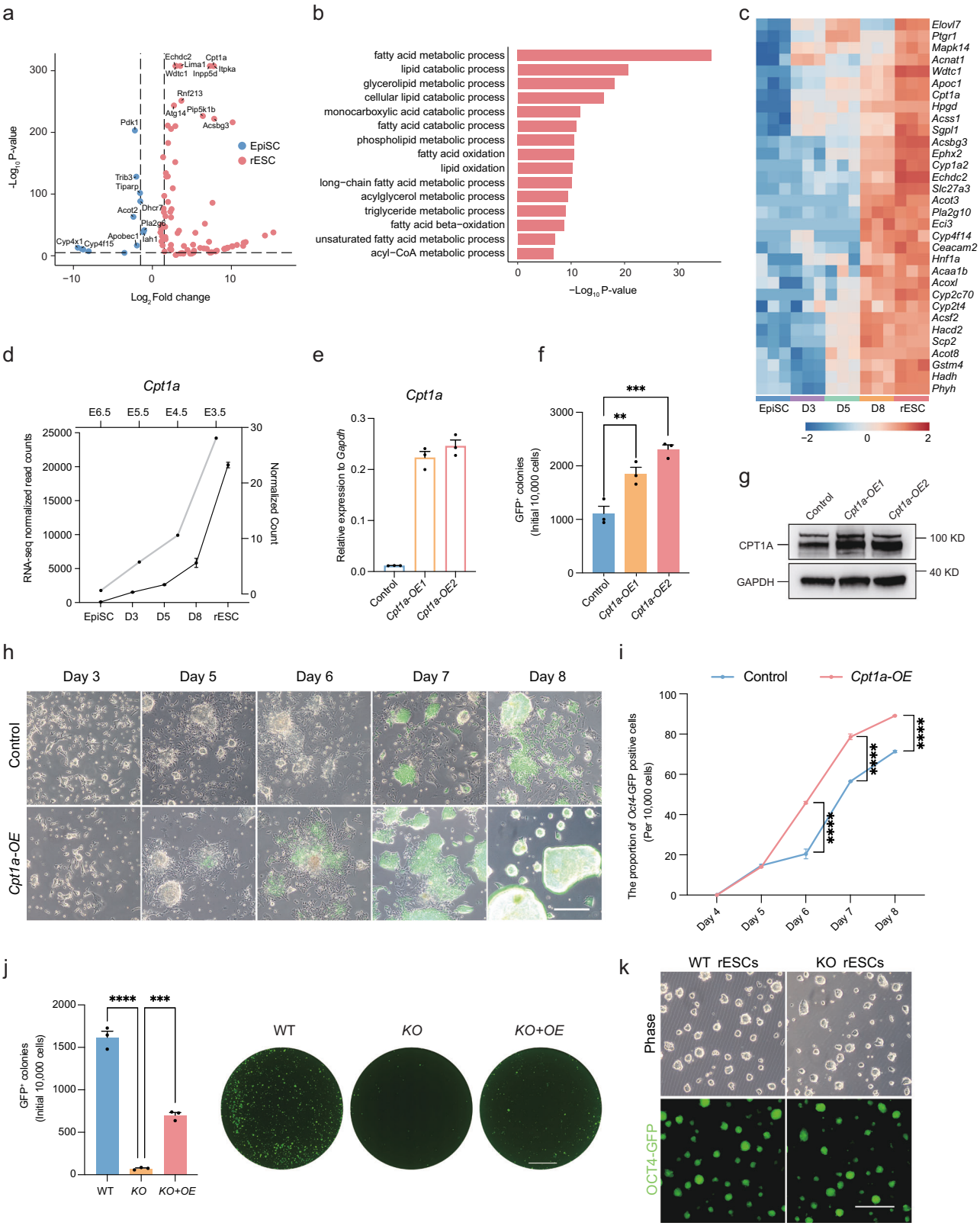

conditions (Supplementary Fig. 8f, g). Moreover, A-485 treatment significantly reduced H3K27ac levels at enhancers and promoters of genes involved in regulating pluripotency and lipid metabolism (Supplementary Fig. 8h). IGV profiling demonstrated that *Cpt1a* enhances H3K27ac at genes crucial for pluripotency, such as *Esrrb*, *Nanog*, *Klf2*, *Nr5a2* and in lipid metabolism genes like *Pparg* and *Cebpa*, with acetylation and transcription levels inhibited by A-485 (Fig. 6g). These findings were further validated through qPCR and immunofluorescence analyses (Fig. 6h-j). Additionally, knockdown of histone acetyltransferases CBP/P300 under OE conditions led to a significant decrease in GFP-positive clones in the BiPNT system, mirroring the effects of A-485 treatment (Fig. 6k). In summary, *Cpt1a* enhanced H3K27 acetylation at chromatin open sites, while inhibition of

Fig. 2 | Expression levels of *Cpt1a* directly affect BiPNT efficiency. a The difference of the transcriptional profiles between EpiSCs and rESCs based on Gene cluster 4 (G4). Significantly upregulated genes in rESCs (compared with EpiSCs, log_2 fold change (log_2 FC > 1.5) are in red, and downregulated (log_2 FC < -1.5) ones are in blue. **b** GO functional enrichment of upregulated genes (from G4) in rESCs. **c** Expression patterns of fatty acid metabolism genes (from **b**) in PNT. Distinct colors represent corresponding timepoints. **d** Comparison of transcriptional profiles between embryonic development (GSE100597) and PNT. **e** RT–qPCR analysis validating the expression of *Cpt1a* between Control and *Cpt1a-OE*. Data are mean ± s.e.m.; $n = 3$ biological replicates. **f** Numbers of *Oct4*-GFP positive colonies for PNT in Control and *Cpt1a-OE*. Data are mean ± s.e.m. Statistical analysis was performed using one-way ANOVA; $n = 3$ biological replicates. *Cpt1a-OE1* vs. Control, **P = 0.0076; Cpt1a-*OE2* vs. Control, **P = 0.0007. Scale bar, 5 mm. **g** Immunoblot analysis of the expression of CPT1A on Day 3. **h** Representative images of PNT between Control and *Cpt1a-OE* at the indicated days. Scale bars, 250μm. **i** FACS analysis of GFP^+ cells at distinct time points during PNT. Data are mean ± s.e.m. Statistical analysis was performed using two-way ANOVA; $n = 3$ biological replicates. ****P < 0.0001. **j** PNT efficiency for the *Cpt1a* knockout or rescue experiments. Data are mean ± s.e.m. Statistical analysis was performed using one-way ANOVA; $n = 3$ biological replicates. WT vs. *KO*, ****P < 0.0001; *KO* + *OE* vs. *KO*, ***P = 0.0001. Scale bar, 5 mm. **k** Images of WT and *Cpt1a-KO* rESCs cultured in 2iL medium. Scale bar, 250μm. The experiments in **g**, **h** and **k** were repeated independently three times with similar results. Source data are provided as Supplementary Data 1.

HATs substantially diminished these acetylation levels, affecting both pluripotency and lipid metabolism.

Discussion

We present evidence that metabolism plays a critical role in the BMP4-driven PNT process (BiPNT)[33,34], accompanied by the metabolic switch and lipid remodeling. We have shown that *Cpt1a* catalyzes lipid remodeling and enhances metabolic activity, providing essential energy and intermediates necessary for cell fate transition, thus advancing the PNT process. Furthermore, acetyl-CoA substantially increases H3K27ac at chromatin open sites, boosting gene expression associated with pluripotency and lipid remodeling (Fig. 7). These findings highlight the essential role of lipid remodeling in cell fate transitions and suggest avenues for further research into the regulatory links between lipid metabolism and epigenetic modifications.

Activated lipid metabolism is a conserved trait in naive mouse and human PSCs, in contrast to the primed state, aligning with in vivo embryonic patterns[5,17–19]. Our data confirm that lipid remodeling is crucial during the PNT transition, mirroring both the intrinsic metabolic state and embryonic development. *Cpt1a* is downregulated during embryonic development and upregulated during PNT, indicating lipid metabolic activity. Prior studies have highlighted its significant role in cellular metabolism[37], proliferation[39], developmental potential[41], and stress response[29], primarily in the naive state. Our work further reveals that *Cpt1a*-driven lipid remodeling during cell fate transitions enhances pluripotency and metabolic shifts. Further investigation is essential to clarify the mechanisms behind *Cpt1a* activation during the PNT and its correspondence with in vivo patterns. Furthermore, it is warranted to explore whether alternative lipid remodeling strategies or genes like *Pparg* and *Cebpa* could similarly facilitate the PNT process or other cell fate transitions.

The role of histone acetylation in regulating pluripotency and determining cell fate has been widely reported[8,64], such as H3K9ac[65], H3K56ac[66,67], and H3K4ac[68]. H3K27ac is commonly used to assess chromatin accessibility and transcriptional activity[8,57,58]. Our prior research underscores its vital function in cell fate transition and pluripotency[57,69–73]. In this work, we demonstrate that *Cpt1a* amplifies metabolic activity and elevates intracellular acetyl-CoA levels, enhancing H3K27ac at chromatin opening sites, thus driving gene transcription and promoting pluripotency transitions. Given the non-specificity of acetyl-CoA acetylation[53], changes in chromatin accessibility may globally alter histone lysine acetylation during the PNT process. Additionally, *Cpt1a* could induce modifications like palmitoylation[74] and participate in lactylation regulation, such as at H3K18[75,76]. Future work involving deep omics analysis will be essential to thoroughly understand these modifications and their effects on metabolic remodeling and cell fate determination.

Methods

Cell culture

Mouse EpiSCs were derived from embryonic day 5.5 mouse embryos generated by mating homozygous *Oct4*-GFP transgenic-allele-carrying mice (CBA/CaJ × C57BL/6J) with 129/Sv female mice[33,34], which were derived from E5.5 mouse embryos in our previous work from the Guangzhou Institutes of Biomedicine and Health, Chinese Academy of Sciences, Guangzhou, China. EpiSCs were maintained without feeders on dishes coated with fetal bovine serum (FBS, OPT500) in N2B27 medium supplemented with bFGF (15 ng/ml, PeproTech), Activin A (20 ng/ml, PeproTech), and XAV939 (1 μM, Selleck) (FAX medium). The N2B27 medium was a mix of equal volumes of DMEM/F12 (GIBCO) and Neurobasal (GIBCO), enriched with 0.5% N2 (GIBCO), 0.5% B27 (GIBCO), 1% GlutaMAX (GIBCO), 1% non-essential amino acids (NEAA) (GIBCO), and 0.1 mM β-mercaptoethanol (GIBCO). EpiSCs, dissociated with Accutase (Sigma), were passaged as single cells in FAX medium with Y27632 (5 μM, Selleck), at approximately 20,000 cells per well in a 12-well plate every 3 days, with daily medium changes.

Mouse ESCs and rESCs were cultured without feeders on dishes coated with 0.1% gelatin. The culture medium used was N2B27 medium, supplemented with 2i/LIF at these final concentrations: PD0325901 (1 μM, TargetMol) and CHIR99021 (3 μM, TargetMol), along with LIF (1,000 U/ml, Millipore). Both mouse ESCs and rESCs were passaged every 3 days using 0.05% trypsin-EDTA (GIBCO) for dissociation.

BMP4-induced Primed-to-Naïve transition system

EpiSCs were reprogrammed into a naïve state using our previously published protocol with slight modifications. EpiSCs were dissociated with Accutase into single cells and seeded at 10,000 cells per well in a 12-well plate coated with FBS in N2B27 + FAX medium, including Y27632 (5 μM). The following day, the medium was replaced with Stage 1 medium, changed daily for 3 days. For the final 5 days, used Stage 2 medium and refreshed daily. The detail components of mediums are as follows:

Stage 1 medium: iCD1 medium[77] containing Vitamin C (50 μg/ml, Sigma), bFGF (10 ng/ml), LiCl (5 mM, Sigma), LIF (1000 U/ml), and CHIR99021 (1 μM), supplemented with BMP4 (10 ng/ml, Proteintech), EPZ6438 (1 μM, TargetMol), EPZ5676 (2.5 μM, TargetMol), Parnate (2 μM, Selleck). In some experiments, we also added A-485 (1 μM, Sigma).

Stage 2 medium: N2B27-2iL medium consisted of N2B27 supplemented with Vitamin C (50 μg/ml), CHIR99021 (3 μM), PD0325901 (1 μM), and LIF (1000 U/ml).

Plasmid construction and lentivirus production

Mouse *Cpt1a* was cloned from the cDNA of ESCs into the pLV-EF1α-IRES-Puro or pKD-EF1α-IRES-Puro expression vector. shRNA inserts were cloned into the pLKO-U6-Puro lentivirus vector. shRNAs sequences were listed in Supplementary Data 2.

For lentivirus generation, HEK293T cells were transfected using either the Ca3(PO4)2 or PEI method. Lentiviral supernatants, concentrated with Lenti-X Concentrator, were used to infect mouse EpiSCs. The infection process included Polybrene (Sigma) treatment for 8 h, and the medium was refreshed with N2B27 + FAX medium for 2 days, followed by selection with puromycin (GIBCO) for 3 days.

Gene knockout in EpiSCs

EpiSC knockout lines were created using the CRISPR-Cas system. gRNAs were designed on https://crispr.mit.edu, then cloned under the human U6 promoter in pX330 (Addgene). To knockout *Cpt1a*, two gRNA pairs were selected to delete critical exons. These gRNA plasmids were transfected into

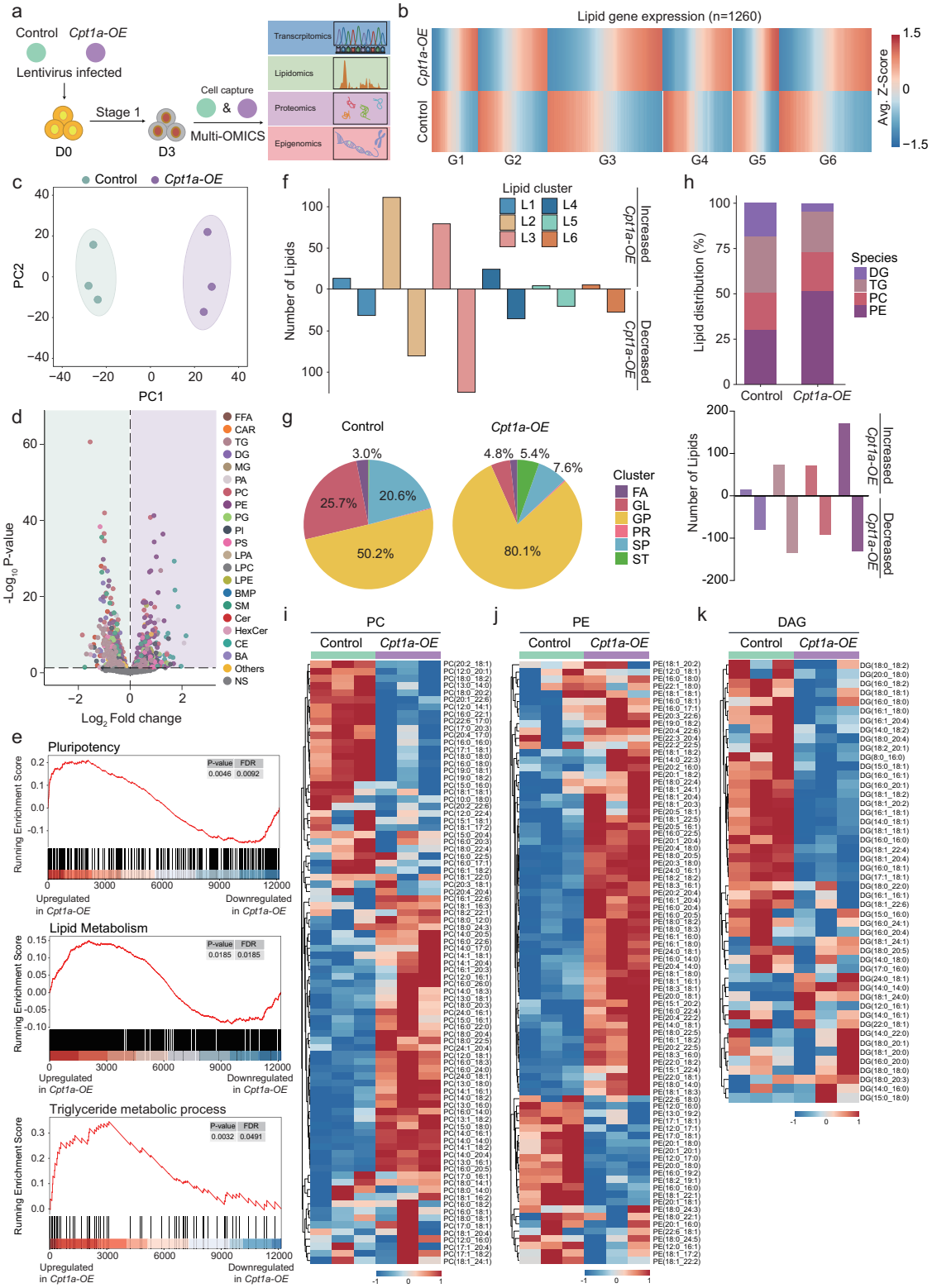

1×10^5 EpiSCs in suspension (N2B27 + FAX medium with 5 μM Y27632) using Lipofectamine 3000 in a 12-well plate. Medium was replaced with fresh N2B27 + FAX medium after 8-10 hours. After 48 hours of transfection, EpiSCs underwent puromycin selection for 3 days, and 1,000 cells were seeded per well in a 6-well plate for colony formation. The individual colonies were identified by genotyping and western blot. gRNAs sequences were listed in Supplementary Data 2.

Quantitative RT-PCR

Total RNA was extracted using FastPure Cell/Tissue Total RNA Isolation Kit V2 (Vazyme, RC112-01). cDNA was synthesized from total RNA using HiScript II Q RT SuperMix for qPCR (Vazyme, R223-01). Real-time quantitative PCR (qPCR) was conducted using ChamQ SYBR Color qPCR Master Mix (Vazyme, Q411-02). Expression levels were normalized to *Gapdh* and analyzed using Microsoft Excel. Each assay was performed in

Fig. 3 | *Cpt1a*-driven lipid remodeling. a Flow chart for multi-omics analysis between Control and *Cpt1a-OE* at Day 3 of the PNT process. **b** Average z-score of lipid-related genes ($n = 1260$) based on *Cpt1a* status (Day 3) stratified by previously defined gene clusters. **c** Principal component analysis of lipidomics distinguishing Control and *Cpt1a-OE*. **d** Volcano plot highlighting differentially abundant lipids (species % of class) in *Cpt1a-OE* of Day 3. Upregulated in OE showing purple. Significantly altered lipids are colored by species (P-value < 0.05). **e** Gene-set enrichment analysis (GSEA) analysis of the lipid metabolism genes, pluripotency genes and triglyceride metabolic process of *Cpt1a-OE* condition comparison to Control. NES = 1.51 in pluripotency; NES = 1.25 in lipid metabolism; NES = 1.78 in triglyceride metabolism. **f** Number of lipid species altered with *Cpt1a* status previously defined lipid clusters. **g** Pie charts comparing the distribution of lipid classes between Control and *Cpt1a-OE* among significant lipids. **h** Top, stacked bar chart showing lipid distribution (% of total) within DG, TG, PC, PE under Control and *Cpt1a-OE* conditions. Bottom, the number of lipid species altered with *Cpt1a* status in the top chart. **i** Heatmap of relative abundance of PC in Control and *Cpt1a-OE* condition. $n = 3$ biological replicates. **j** Heatmap of relative abundance of PE in Control and *Cpt1a-OE* condition. $n = 3$ biological replicates. **k** Heatmap of relative abundance of DG in Control and *Cpt1a-OE* condition. $n = 3$ biological replicates. Source data are provided as Supplementary Data 1.

technical triplicates. The primers used for RT-qPCR are detailed in Supplementary Data 2.

Western blot

Cells were collected and lysed in RIPA buffer (Sigma) containing protease inhibitor cocktail (Roche) on ice for 15 minutes. After centrifugation, the supernatants were mixed with loading buffer, subjected to SDS-PAGE, and then transferred to membranes. The proteins were probed with primary and secondary antibodies for detection. The antibodies used included anti-CPT1A (Proteintech, no. 15184-1-AP, 1:5000), anti-GAPDH (CST, no. 2118, 1:2000), and anti-H3K27ac (Abcam, no. ab4729, 1:1000), anti-H3 (Abcam, no. ab1791, 1:1000).

Immunofluorescence

Cells growing in the chamber (ibidi, 80841) were washed thrice with PBS and fixed in 4% PFA (Beyotime) for 30 minutes. They were then permeabilized and blocked using 0.1% Triton X-100 (Sigma) and 3% BSA (Sigma) for 30 minutes at room temperature. Following this, cells were incubated with the primary antibody overnight at 4 °C. After five PBS washes and 1-hour incubation with secondary antibodies, cells were stained with DAPI (Sigma, D9542) for 5 minutes. Coverslips were then mounted on slides for imaging using a confocal microscope (Zeiss LSM 900). Fluorescence intensity was analyzed using Zeiss software. The antibodies used included anti-CPT1A (Proteintech, no. 66039-1-Ig, 1:25), anti-TOMM20 (Abcam, no. ab186735, 1:100), anti-H3K27ac (Abcam, no. ab4729, 1:200) and anti-Acetylated-Lysine (CST, no. 9441, 1:200).

Flow cytometry

Cells were dissociated into single cells with 0.25% trypsin-EDTA (GIBCO), followed by centrifugation for collection. After a PBS wash, cells were resuspended in N2B27 medium and filtered with a 40 μm cell strainer to remove large clumps of cells. Cells were analyzed with CytoFLEXLX 6L (Beckmen) and sorted using BD FACSAria Fusion (BD Biosciences), with GFP fluorescence detected in the FITC channel. Data analysis was carried out using FlowJo v.10.8.1. The gating strategy for FACS analysis are provided in Supplementary information.

Cell viability assay

Control and *Cpt1a-OE* EpiSC cells were seeded in 96-well plates (1,000 cells per well, CORNING, 3610) using N2B27 + FAX medium. rESC cells were seeded in 96-well plates (5,000 cells per well, CORNING, 3610) using N2B27 + 2iL medium. After 72 hours, cell viability was assessed using either the Cell Counting Kit-8 (CCK8, Beyotime, C0039) or the CellTiter-Lumi™ Luminescent Cell Viability Assay Kit (CTL II, Beyotime, C0056), following manufacturer protocols. For CCK8, 10 μl of the solution was added to each well and incubated for 1 hour, and absorbance at 450 nm was measured using a spectrophotometer. For CellTiter-Lumi™, 100 μl of the solution was added, plates were shaken for 2 minutes, incubated for 10 minutes, and luminescence was measured using a luminometer.

Mitochondrial imaging

Cells were plated in the chamber (ibidi, 80826) and incubated with Mito-Tracker Green (200 nM, Thermo Fisher Scientific, A66468) for 45 minutes (37 °C) on the third day of the BiPNT process to stain mitochondria. After washing with culture medium, mitochondrial morphology was visualized using a 488 nm laser scanning confocal microscope (Zeiss LSM 900). The mitochondrial aspect ratio was quantified by measuring the length and width with ImageJ software.

Seahorse XF assay for Oxygen Consumption Rate (OCR)

Cells were initially induced in the BiPNT system until Day 2, then dissociated using accutase (STEM CELL) and seeded into pre-prepared 96-well plates (40,000 cells per well, Agilent, 103793). Cells were cultured in Stage 1 medium at 37 °C in a CO_2 incubator on Day 3. On the assay day, the culture medium was removed and replaced with Seahorse XF Assay Medium (180 μl/well, Agilent, 103575) containing glutamine (2 mM, Agilent, 103579), pyruvate (5 mM, Agilent, 103578), and glucose (10 mM, Agilent, 103577). Simultaneously, the probe plate was filled with Seahorse Calibrant (200 μl/well, Agilent, 100840). The cell plate and probe plate were then placed in a no-CO_2 incubator at 37 °C for 1 hour. The oxygen consumption rate (OCR) was performed with the Seahorse XFe96 Analyzer, and measured using the Mito Stress Test kit (Agilent, 103015), with injections of the following inhibitors: oligomycin (1.5 μM), FCCP (2 μM), rotenone, and antimycin A (0.5 μM).

Acetyl-CoA measurement with LC-MS

Cells were plated in a 6-well plate and induced in the BiPNT system until Day 3. Vacuum aspirated off medium and washed with cold PBS three times. Immediately add 800 ul of methanol (-80 °C) to the plate and transfer to -80 °C freezer for 1 h. Then, scraped plates on dry ice with a cell scraper and transferred the cell lysate/methanol mixture to 1.5 ml centrifuge tubes. After the centrifuge (9000 *g*, 4 °C, 10 min), transfer supernatants to new 1.5 centrifuge tubes on dry ice. Quantitative analysis with LC-MS from Mass Spectrometry & Metabolomics Platform, Biomedical Research Core Facilities, Westlake University, Hangzhou, China. Acetyl-CoA Standard from Acetyl-Coenzyme A Assay Kit (Sigma, MAK039).

Lipidomics assay

Cells were collected from specific conditions or at designated timepoints. Lipid metabolites were extracted from 5×10^6 cells per sample. The extraction of metabolites and LC-MS/MS analysis were primarily conducted by Metware Biotechnology Co., Ltd., Wuhan, China. Briefly, Cells sourced at particular timepoints and under various conditions undergo washing with cold PBS and centrifugation (500 *g*, 4 °C, 5 min). The cells were then exposed to freeze-thaw cycles, mixed with a methanol and MTBE solution, and centrifuged again (12000 r/min, 4 °C, 10 min). The supernatant was concentrated, redissolved in mobile phase B, and used for LC-MS/MS analysis. Chromatographic peaks are normalized to facilitate both qualitative and relative quantitative analysis. Quality control samples are prepared by mixing sample extracts to test reproducibility.

Metabolomics assay

Cells obtained from specific conditions or designated time points (5×10^6 cells per sample) underwent PBS washing and centrifugation (500 *g*, 4 °C, 5 min). The resulting pellet was combined with a 70% methanol aqueous solution, subjected to freeze-thaw cycles, and then centrifuged (12000 r/min, 4 °C, 10 min). The supernatant obtained was collected into sample bottles for LC-ESI-MS/MS analysis. Chromatographic peaks were normalized, enabling both qualitative and relative quantitative analysis. The entire

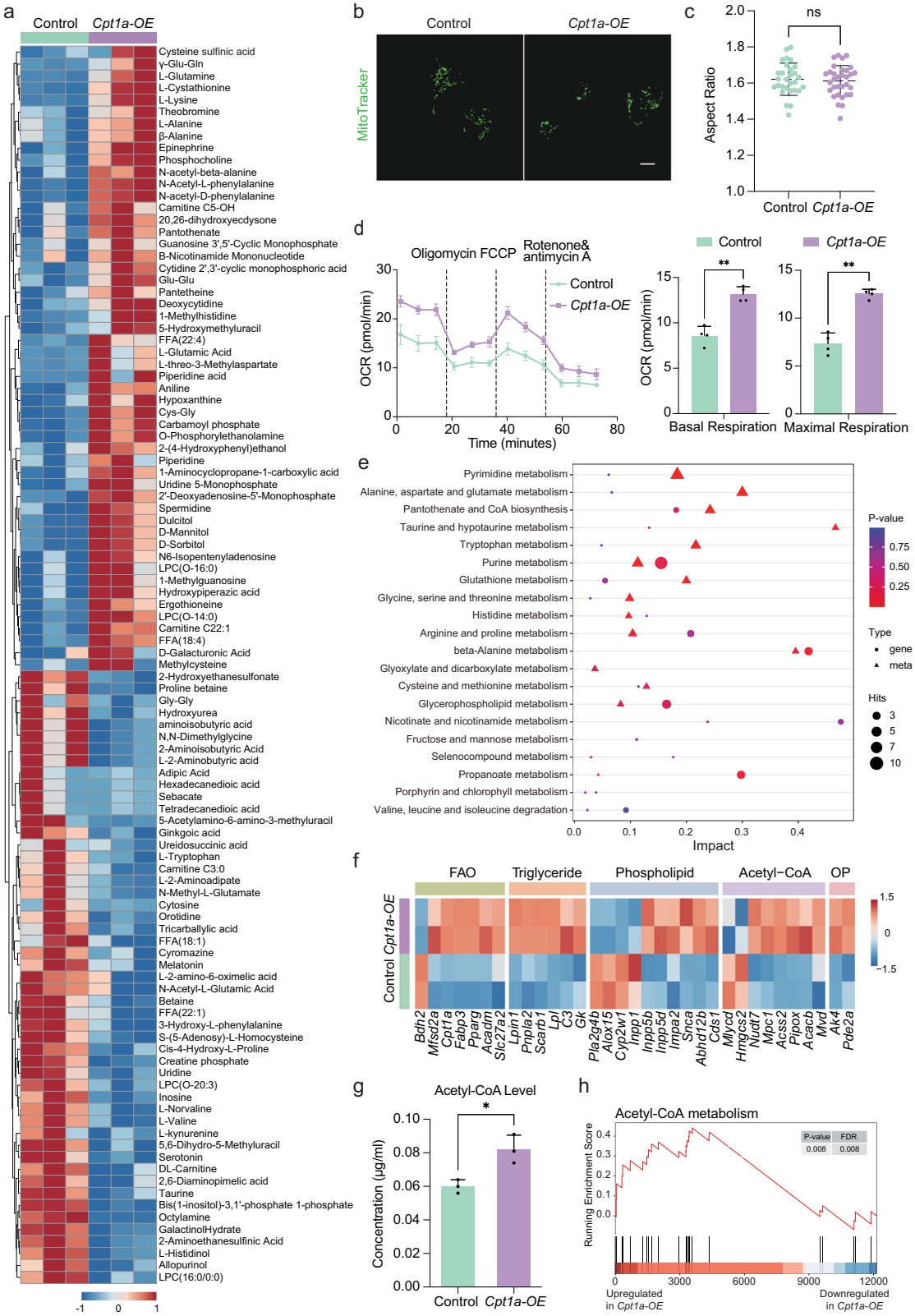

process, including metabolite extraction and analysis, was conducted by Metware Biotechnology Co., Ltd., Wuhan, China.

Bulk RNA-seq and expression analysis

Total RNA was extracted from the samples. Sequencing libraries were then prepared following the protocol of the VAHTS mRNA-seq v2 Library Prep Kit for Illumina (Vazyme, NR601-01/02). The prepared libraries were sequenced using the NextSeq 500 High Output Kit v2 (75 cycles; Illumina, FC-404-1005).

RNA-seq reads were aligned to the mm10 transcriptome index. For the time course, reads were aligned with HiSAT2[78] software. Raw counts were extracted with StringTie[79]. For the rest of the samples, reads were

Fig. 4 | *Cpt1a*-driven metabolic reprogramming. a Heatmap of relative abundance of differential metabolites in Control and *Cpt1a-OE* condition. $n = 3$ biological replicates. **b** Representative confocal images of mitochondria on Day 3 of the BiPNT system, under Control or *Cpt1a-OE* conditions and subsequently stained with MitoTracker Green. Scale bar, 10μm. **c** Quantification of mitochondrial length by aspect ratio on Day 3 of the BiPNT system, under Control or *Cpt1a-OE* conditions as shown in (A). Data are mean ± s.e.m. Statistical analysis was performed using a two-sided unpaired t-test; $n = 29$ cells from Control and $n = 32$ cells from OE condition. ns, non-significant. **d** Oxygen consumption rate (OCR) trace of Control and *Cpt1a-OE* conditions in Day 3. Data are mean ± s.d. Statistical analysis was performed using a two-sided unpaired t-test; $n = 4$ technical replicates from one of two independent experiments. Basal respiration $^{**}P = 0.0091$, Max respiration $^{**}P = 0.0025$. **e** KEGG pathway analysis of significantly changed metabolites and genes using MetaboAnalyst. Shape indicates type of omics; Size for counts of features; Color for significance. **f** Heatmap of the expression difference of representative metabolic genes altered with *Cpt1a* status. FAO, fatty acid oxidation; OP, oxidative phosphorylation; and other means of metabolic process. Different colors represent corresponding metabolic pathways. **g** The concentration of acetyl-CoA in Control and *Cpt1a-OE* conditions was measured by LC-MS. Data are mean ± s.d. $n = 3$ biological replicates. $^{*}P = 0.0151$. **h** GSEA analysis of acetyl-CoA metabolic genes of *Cpt1a-OE* condition comparison to Control. NES = 1.81. Source data are provided as Supplementary Data 1.

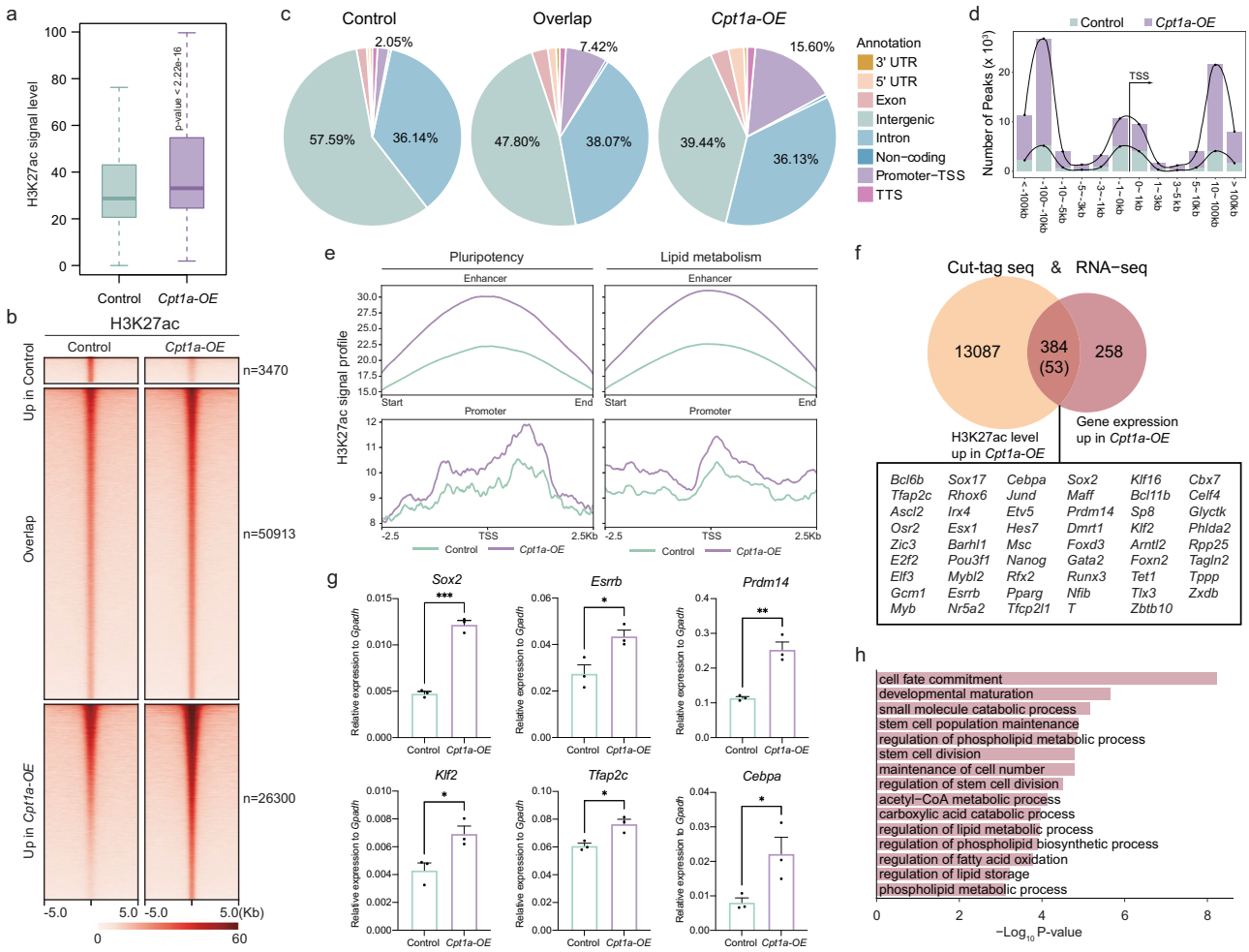

Fig. 5 | Overexpression of *Cpt1a* augments H3K27 acetylation. a Global signal of H3K27ac between Control and *Cpt1a-OE* conditions. Boxplots denote the medians and the interquartile ranges (IQR). P-value from two-sided Student's *t*-test. **b** Heatmap illustrating the density of H3K27ac binding sites on Day 3 under Control or *Cpt1a-OE* conditions, showing all binding events centered on the peak region within a 5 kb window around the peak. **c** Pie charts showing the genomic distribution of the peaks identified by H3K27ac in Control, *Cpt1a-OE* and Overlap. **d** Bar chart showing the distance from H3K27ac-binding sites to TSSs in Control and *Cpt1a-OE*. **e** Average profiles of H3K27ac signals at enhancer and promoter showing the H3K27ac level changes upon *Cpt1a-OE* at the pluripotent and lipid metabolic genes. **f** Venn diagram indicating the number of genes up-regulated at both H3K27ac and transcriptional levels in *Cpt1a-OE*. 53 transcription factors are listed in the bottom box. **g** RT-qPCR analysis for expression of Naïve pluripotent markers and lipid metabolic genes in Control and *Cpt1a-OE* conditions at Day 3 of BiPNT. Data are mean ± s.e.m. Statistical analysis was performed using a two-sided unpaired t-test; $n = 3$ biological replicates. $^{*}p < 0.05$, $^{**}p < 0.01$, $^{***}p < 0.001$, $^{****}p < 0.0001$. **h** Functional enrichment analysis of the overlapped genes in **f**. Source data are provided as Supplementary Data 1.

aligned with STAR aligner[80]. Raw counts were extracted with scTE[81]. Genes with low counts were removed. Median of ratios method was used for normalization. Differential expression analysis was done with DESeq2[82]. Gene ontology analysis and GSEA were performed with clusterProfiler[83–85]. pheatmap was applied to generate heatmaps. Clustering was done using pheatmap with *k*-means. Volcano plots were generated using Enhanced-Volcano. rowMeans() was used to calculate mean expression for each sample. RNA-seq reads for early embryo development in Fig. 2d were from GSE100597[40].

CUT&Tag data analysis

The CUT&Tag libraries were constructed using the Hyperactive In-Situ ChIP Library Prep Kit for Illumina (pG-Tn5) (Vazyme, TD901) and the TruePrep Index Kit V2 for Illumina (Vazyme, TD202). Approximately

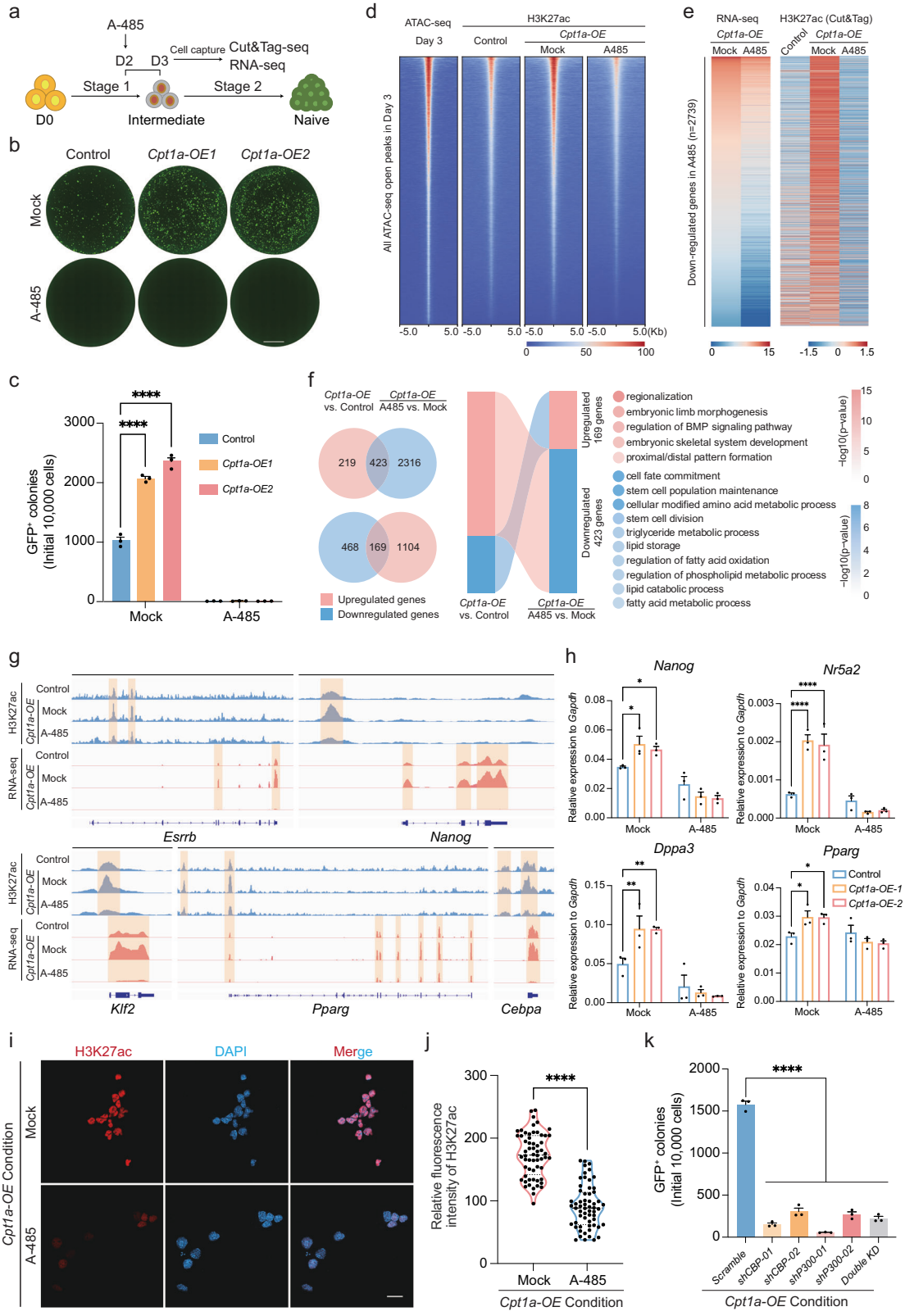

100,000 live cells were collected for each sample. The antibodies used anti-H3K27ac (Abcam, no. ab4729, 1:50). The prepared CUT&Tag libraries were sequenced on an Illumina Nova6000 platform by Novogene Co., Ltd., Beijing, China.

Adapters were first trimmed by TrimGalore. Cleaned reads were aligned to mm10 mouse genome with Bowtie2(--very-sensitive --end-to-end --no-unal --phred33 --no-mixed -X2000)[86]. Bigwig files were generated by bamCoverage module in deepTools[87], with RPKM normalization. Peaks were called by MACS2[88]. bedtools were used to classified peaks[89]. annotatePeaks.pl from HOMER[90] was used to annotate peaks. Heatmaps and profiles were generated by deepTools. Biological replicates were merged. Integrative Genomic Viewer (IGV)[91]was used to visualize read coverage on

Fig. 6 | A-485 disrupts lipid remodeling and pluripotent gene expression, significantly reducing PNT efficiency. a Schematic of A-485 treated on Day 2 and removed on Day 3 for further analysis. A-485 work concentration = 1 μM. **b** Whole well fluorescent images of resetting cultures with the protocol in without or with A-485 treatment. Scale bars, 5 mm. The experiments were repeated independently three times with similar results. **c** Quantification for **b**. Data are mean ± s.e.m. Statistical analysis was performed using two-way ANOVA; $n = 3$ biological replicates. *Cpt1a-OE1* vs. Control in Mock ****$p < 0.0001$, *Cpt1a-OE2* vs. Control in Mock ****$p < 0.0001$, ns, non-significant. **d** Heatmap showing ATAC-seq signals at open chromatin sites on Day 3 of the BiPNT system, alongside corresponding H3K27ac signals at these ATAC-seq peaks, under control conditions and OE conditions treated without or with A-485. **e** Heatmap showing down-regulated genes after A-485 treatment under OE conditions, along with corresponding H3K27ac signals for these down-regulated genes. **f** Left, Venn diagrams showing DEGs in both *Cpt1a-OE* (relative to Control) and A-485 treatment in OE condition (relative to Mock). Right, Sankey plot showing rescued genes in A-485 treatment. GO term and pathway enrichment analyses for upregulated (red) and downregulated DEGs (blue) are displayed on the right. Enrichment levels are presented with different color intensities. **g** Cut&Tag seq (H3K27ac) and RNA-seq tracks of indicated genes in Day 3 BiPNT cells without or with A-485 treatment. **h** RT-qPCR analysis for expression of Naïve pluripotent markers and lipid metabolic genes at Day 3 of BiPNT without or with A-485 treatment. Data are mean ± s.e.m. Statistical analysis was performed using two-way ANOVA; $n = 3$ biological replicates. *$p < 0.05$, **$p < 0.01$, ***$p < 0.001$, ****$p < 0.0001$. **i** Immunostaining of H3K27ac in Day 3 BiPNT cells without or with A-485 treatment. Scale bars, 20μm. **j** Immunostaining quantification of H3K27ac relative intensities in **i**. Statistical analysis was performed using a two-sided unpaired t-test; $n = 60$ cells from Mock and $n = 60$ cells from A485 condition. ****$p < 0.0001$. **k** Numbers of *Oct4*-GFP positive colonies with Scramble and *shCBP/P300* in OE conditions. Data are mean ± s.e.m. Statistical analysis was performed using one-way ANOVA; $n = 3$ biological replicates. ****$P < 0.0001$. Source data are provided as Supplementary Data 1.

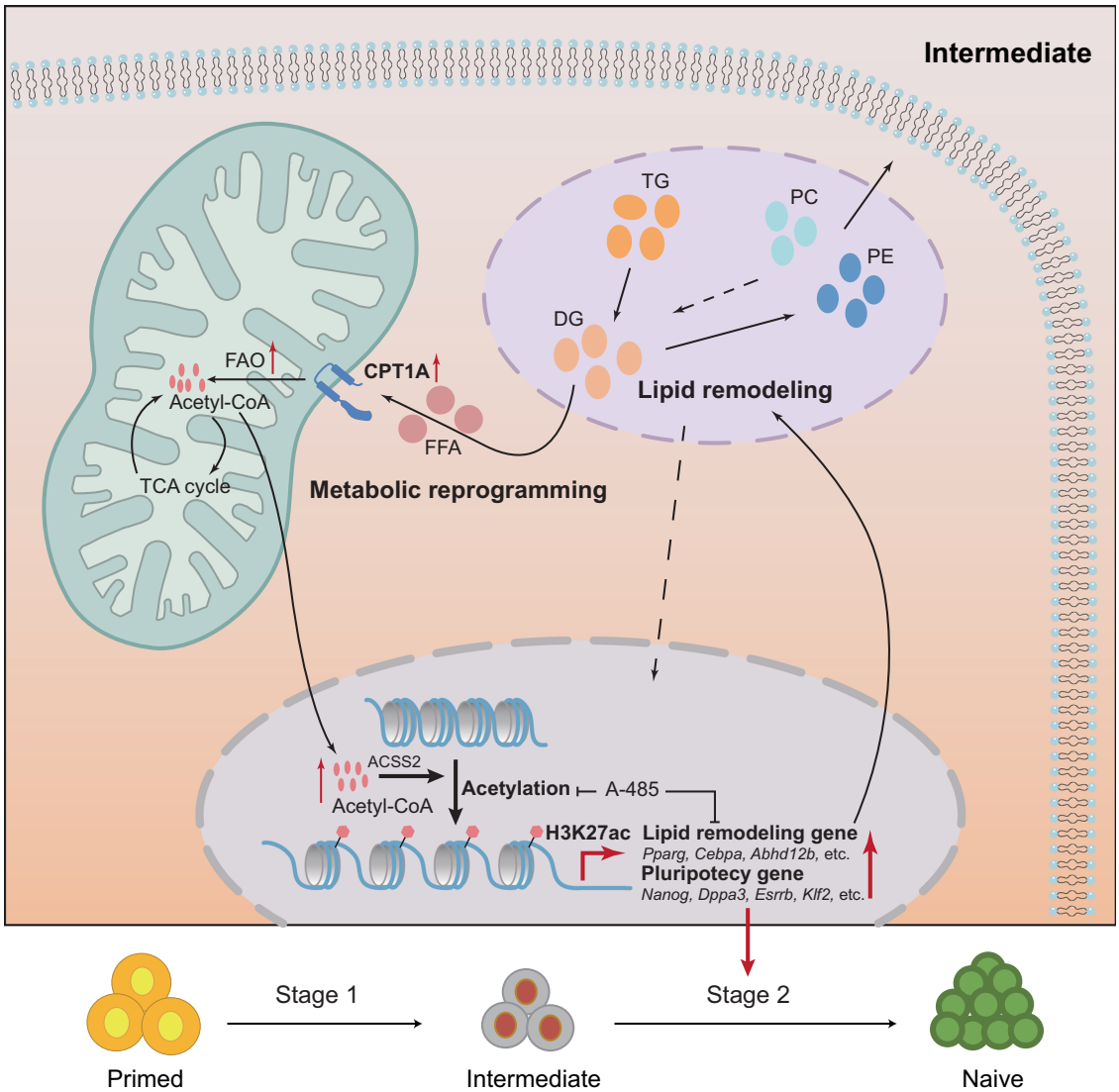

Fig. 7 | Schematic diagram of lipid remodeling drives BiPNT. In BiPNT, *Cpt1a*-driven lipid remodeling and metabolic reprogramming are essential. Glycerides like TG and DG are active in metabolism, some transform into FFAs for *Cpt1a*-mediated mitochondrial fatty acid oxidation, yielding acetyl-CoA. The rest contribute to glycerophospholipids like PE and PC synthesis for cellular functions. Acetyl-CoA not only contributes to the TCA cycle and metabolic activation but also triggers an increase in histone acetylation. Conversely, the histone acetyltransferase (HAT) inhibitor A-485 impedes histone acetylation, thereby inhibiting lipid remodeling and the BiPNT process. Therefore, *Cpt1a* drives the BiPNT process by promoting lipid remodeling and enhancing histone acetylation.

the genome. Other analysis was done by bedtools. Average profiles were produced via computeMatrix and plotProfile modules in deepTools[87]. Biological replicates were merged.

Lipidomics and metabolomics analysis

Differential metabolites were calculated by running DESeq2. Volcano plots were generated using EnhancedVolcano. KEGG analysis for metabolites was performed using MetaboAnalyst with KEGG ID for each metabolite.

Lipid-gene pair analysis

Pearson correlation was calculated based on lipid species and gene expression data. Here, lipid metabolic genes were selected for correlation analysis. Clustering was done using pheatmap with hierarchical clustering. Lipid clusters were annotated according to enrichment analysis done by hypergeometric test. Enrichment score for lipid clusters was obtained through $\log_{10}$ transformation on P-value. Lipid metabolic genes were obtained from Reactome[92] and GO.

Statistical analysis

No specific statistical method was employed to predetermine the sample size. The experiments were conducted without randomization, and allocation during experimentation and outcome assessment was not blinded to the investigators. Data are represented as mean ± standard deviation (s.d.) or mean ± standard error of the mean (s.e.m.). P-values were determined using two-tailed unpaired Student's t-tests, one-way ANOVA, or two-way ANOVA, executed with GraphPad Prism 10 software. *P*-value less than 0.05 was considered statistically significant, denoted as $^{*}P < 0.05$, $^{**}P < 0.01$, $^{***}P < 0.001$, $^{****}P < 0.0001$. Detailed information on the statistical test used, exact P-values, sample sizes, and the number of independent experiments are provided in the figure legends.

Reporting summary

Further information on research design is available in the Nature Portfolio Reporting Summary linked to this article.

Data availability

RNA-seq and Cut&Tag-seq data that support the findings of this study have been deposited in the Gene Expression Omnibus[75] under accession codes GSE253147. The metabolomics and lipidomics data are available on Zenodo with the following: https://zenodo.org/doi/10.5281/zenodo.13358096. The mass spectrometry proteomics data have been deposited to the ProteomeXchange Consortium (http://proteomecentral.proteomexchange.org) via the iProX partner repository with the dataset identifier PXD048820. Source data are provided as Supplementary Data 1. Supplementary Data 2 is the primers/sequences used in this study. Uncropped and unedited blot images are provided as Supplementary information files. The authors declare that all data supporting the findings of this study are available within the article and its Supplementary information files or from the corresponding author upon reasonable request. Source data are provided with this paper.

Received: 8 March 2024; Accepted: 10 September 2024;
Published online: 30 September 2024

References

1. Wu, J., Ocampo, A. & Belmonte, J. C. I. Cellular metabolism and induced pluripotency. *Cell* **166**, 1371–1385 (2016).
2. Ryall, J. G., Cliff, T., Dalton, S. & Sartorelli, V. Metabolic reprogramming of stem cell epigenetics. *Cell Stem Cell* **17**, 651–662 (2015).
3. Liu, K., Cao, J., Shi, X., Wang, L. & Zhao, T. Cellular metabolism and homeostasis in pluripotency regulation. *Protein Cell* **11**, 630–640 (2020).
4. Zhang, J. et al. Metabolism in Pluripotent stem cells and early mammalian development. *Cell Metab.* **27**, 332–338 (2018).
5. Sperber, H. et al. The metabolome regulates the epigenetic landscape during naive-to-primed human embryonic stem cell transition. *Nat. Cell Biol.* **17**, 1523–1535 (2015).
6. TeSlaa, T. et al. alpha-Ketoglutarate accelerates the initial differentiation of primed human pluripotent stem cells. *Cell Metab.* **24**, 485–493 (2016).
7. Sun, H. et al. Metabolic switch and epithelial-mesenchymal transition cooperate to regulate pluripotency. *EMBO J.* **39**, e102961 (2020).
8. Li, L. et al. Glis1 facilitates induction of pluripotency via an epigenome-metabolome-epigenome signalling cascade. *Nat. Metab.* **2**, 882–892 (2020).
9. Zhao, J. et al. Metabolic remodelling during early mouse embryo development. *Nat. Metab.* **3**, 1372–1384 (2021).
10. Li, W. et al. Nuclear localization of mitochondrial TCA cycle enzymes modulates pluripotency via histone acetylation. *Nat. Commun.* **13**, 7414 (2022).
11. Hwang, I. Y. et al. Psat1-dependent fluctuations in alpha-Ketoglutarate affect the timing of ESC differentiation. *Cell Metab.* **24**, 494–501 (2016).
12. Carey, B. W., Finley, L. W., Cross, J. R., Allis, C. D. & Thompson, C. B. Intracellular alpha-ketoglutarate maintains the pluripotency of embryonic stem cells. *Nature* **518**, 413–416 (2015).
13. Wu, Y. et al. Phospholipid remodeling is critical for stem cell pluripotency by facilitating mesenchymal-to-epithelial transition. *Sci. Adv.* **5**, eaax7525 (2019).
14. Zhang, L. et al. Low-input lipidomics reveals lipid metabolism remodelling during early mammalian embryo development. *Nat. Cell Biol.* **26**, 278–293 (2024).
15. Santos, A. L. & Preta, G. Lipids in the cell: organisation regulates function. *Cell Mol. Life Sci.* **75**, 1909–1927 (2018).
16. Olzmann, J. A. & Carvalho, P. Dynamics and functions of lipid droplets. *Nat. Rev. Mol. Cell Biol.* **20**, 137–155 (2019).
17. Cornacchia, D. et al. Lipid deprivation induces a stable, naive-to-primed intermediate state of pluripotency in human PSCs. *Cell Stem Cell* **25**, 120–136.e110 (2019).
18. Aizawa, R. et al. Synthesis and maintenance of lipid droplets are essential for mouse preimplantation embryonic development. *Development* **146**, dev181925 (2019).
19. Arena, R. et al. Lipid droplets in mammalian eggs are utilized during embryonic diapause. *Proc. Natl Acad. Sci. USA* **118**, e2018362118 (2021).
20. Nichols, J. & Smith, A. Naive and primed pluripotent states. *Cell Stem Cell* **4**, 487–492 (2009).
21. Perestrelo, T., Correia, M., Ramalho-Santos, J. & Wirtz, D. Metabolic and mechanical cues regulating pluripotent stem cell fate. *Trends Cell Biol.* **28**, 1014–1029 (2018).
22. Brons, I. G. et al. Derivation of pluripotent epiblast stem cells from mammalian embryos. *Nature* **448**, 191–195 (2007).
23. Tesar, P. J. et al. New cell lines from mouse epiblast share defining features with human embryonic stem cells. *Nature* **448**, 196–199 (2007).
24. Bao, S. et al. Epigenetic reversion of post-implantation epiblast to pluripotent embryonic stem cells. *Nature* **461**, 1292–1295 (2009).
25. Guo, G. & Smith, A. A genome-wide screen in EpiSCs identifies Nr5a nuclear receptors as potent inducers of ground state pluripotency. *Development* **137**, 3185–3192 (2010).
26. Guo, G. et al. Klf4 reverts developmentally programmed restriction of ground state pluripotency. *Development* **136**, 1063–1069 (2009).
27. Zhou, H. et al. Conversion of mouse epiblast stem cells to an earlier pluripotency state by small molecules. *J. Biol. Chem.* **285**, 29676–29680 (2010).
28. Zhou, W. et al. HIF1alpha induced switch from bivalent to exclusively glycolytic metabolism during ESC-to-EpiSC/hESC transition. *EMBO J.* **31**, 2103–2116 (2012).
29. Yan, H. et al. Fatty acid oxidation is required for embryonic stem cell survival during metabolic stress. *EMBO Rep.* **22**, e52122 (2021).

30. Gu, W. et al. Glycolytic metabolism plays a functional role in regulating human pluripotent stem cell state. *Cell Stem Cell* **19**, 476–490 (2016).
31. Stuart, H. T. et al. Distinct molecular trajectories converge to induce naive pluripotency. *Cell Stem Cell* **25**, 388–406 e388 (2019).
32. Du, P. et al. An intermediate pluripotent state controlled by MicroRNAs is required for the naive-to-primed stem cell transition. *Cell Stem Cell* **22**, 851–864.e855 (2018).
33. Yu, S. et al. BMP4 resets mouse epiblast stem cells to naive pluripotency through ZBTB7A/B-mediated chromatin remodelling. *Nat. Cell Biol.* **22**, 651–662 (2020).
34. Yu, S. et al. BMP4 drives primed to naive transition through PGC-like state. *Nat. Commun.* **13**, 2756 (2022).
35. Birsoy, K. et al. An essential role of the mitochondrial electron transport chain in cell proliferation is to enable aspartate synthesis. *Cell* **162**, 540–551 (2015).
36. Minami, J. K. et al. CDKN2A deletion remodels lipid metabolism to prime glioblastoma for ferroptosis. *Cancer Cell* **41**, 1048–1060.e1049 (2023).
37. Hao, F. et al. Butyrate enhances CPT1A activity to promote fatty acid oxidation and iTreg differentiation. *Proc. Natl Acad. Sci. USA* **118**, e2014681118 (2021).
38. Mihaylova, M. M. et al. Fasting activates fatty acid oxidation to enhance intestinal stem cell function during homeostasis and aging. *Cell Stem Cell* **22**, 769–778.e764 (2018).
39. Tang, M. et al. CPT1A-mediated fatty acid oxidation promotes cell proliferation via nucleoside metabolism in nasopharyngeal carcinoma. *Cell Death Dis.* **13**, 331 (2022).
40. Mohammed, H. et al. Single-cell landscape of transcriptional heterogeneity and cell fate decisions during mouse early gastrulation. *Cell Rep.* **20**, 1215–1228 (2017).
41. Nyman, L. R. et al. Homozygous carnitine palmitoyltransferase 1a (liver isoform) deficiency is lethal in the mouse. *Mol. Genet. Metab.* **86**, 179–187 (2005).
42. Gu, L. et al. Targeting Cpt1a-Bcl-2 interaction modulates apoptosis resistance and fibrotic remodeling. *Cell Death Differ.* **29**, 118–132 (2022).
43. Huang, D. et al. Multiomic analysis identifies CPT1A as a potential therapeutic target in platinum-refractory, high-grade serous ovarian cancer. *Cell Rep. Med.* **2**, 100471 (2021).
44. Luo, M. et al. Overexpression of carnitine palmitoyltransferase 1A promotes mitochondrial fusion and differentiation of glioblastoma stem cells. *Lab. Invest.* **102**, 722–730 (2022).
45. Ngo, J. et al. Mitochondrial morphology controls fatty acid utilization by changing CPT1 sensitivity to malonyl-CoA. *EMBO J.* **42**, e111901 (2023).
46. Yuan, Q. et al. CPT1alpha maintains phenotype of tubules via mitochondrial respiration during kidney injury and repair. *Cell Death Dis.* **12**, 792 (2021).
47. Lisowski, P., Kannan, P., Mlody, B. & Prigione, A. Mitochondria and the dynamic control of stem cell homeostasis. *EMBO Rep* **19**, e45432 (2018).
48. Bahat, A. et al. MTCH2-mediated mitochondrial fusion drives exit from naive pluripotency in embryonic stem cells. *Nat. Commun.* **9**, 5132 (2018).
49. Moussaieff, A. et al. Glycolysis-mediated changes in acetyl-CoA and histone acetylation control the early differentiation of embryonic stem cells. *Cell Metab.* **21**, 392–402 (2015).
50. He, W., Li, Q. & Li, X. Acetyl-CoA regulates lipid metabolism and histone acetylation modification in cancer. *Biochim Biophys. Acta Rev. Cancer* **1878**, 188837 (2023).
51. Zhu, X. et al. Acetate controls endothelial-to-mesenchymal transition. *Cell Metab.* **35**, 1163–1178 e1110 (2023).
52. Bishop, T. R. et al. Acetyl-CoA biosynthesis drives resistance to histone acetyltransferase inhibition. *Nat. Chem. Biol.* **19**, 1215–1222 (2023).
53. Barnes, C. E., English, D. M. & Cowley, S. M. Acetylation & Co: an expanding repertoire of histone acylations regulates chromatin and transcription. *Essays Biochem.* **63**, 97–107 (2019).
54. Dieterich, I. A. et al. Acetyl-CoA flux regulates the proteome and acetyl-proteome to maintain intracellular metabolic crosstalk. *Nat. Commun.* **10**, 3929 (2019).
55. Wu, Y. et al. Plin2-mediated lipid droplet mobilization accelerates exit from pluripotency by lipidomic remodeling and histone acetylation. *Cell Death Differ.* **29**, 2316–2331 (2022).
56. Nair, V. D. et al. Differential analysis of chromatin accessibility and gene expression profiles identifies cis-regulatory elements in rat adipose and muscle. *Genomics* **113**, 3827–3841 (2021).
57. Wang, B. et al. The NuRD complex cooperates with SALL4 to orchestrate reprogramming. *Nat. Commun.* **14**, 2846 (2023).
58. Wang, M., Chen, Z. & Zhang, Y. CBP/p300 and HDAC activities regulate H3K27 acetylation dynamics and zygotic genome activation in mouse preimplantation embryos. *EMBO J.* **41**, e112012 (2022).
59. Kaya-Okur, H. S., Janssens, D. H., Henikoff, J. G., Ahmad, K. & Henikoff, S. Efficient low-cost chromatin profiling with CUT&Tag. *Nat. Protoc.* **15**, 3264–3283 (2020).
60. Kaya-Okur, H. S. et al. CUT&Tag for efficient epigenomic profiling of small samples and single cells. *Nat. Commun.* **10**, 1930 (2019).
61. Lasko, L. M. et al. Discovery of a selective catalytic p300/CBP inhibitor that targets lineage-specific tumours. *Nature* **550**, 128–132 (2017).
62. Sungalee, S. et al. Histone acetylation dynamics modulates chromatin conformation and allele-specific interactions at oncogenic loci. *Nat. Genet.* **53**, 650–662 (2021).
63. Bowers, E. M. et al. Virtual ligand screening of the p300/CBP histone acetyltransferase: identification of a selective small molecule inhibitor. *Chem. Biol.* **17**, 471–482 (2010).
64. Zhou, W. et al. Acetylation of H3K4, H3K9, and H3K27 mediated by p300 regulates the expression of GATA4 in cardiocytes. *Genes Dis.* **6**, 318–325 (2019).
65. Du, Y. et al. Nucleosome eviction along with H3K9ac deposition enhances Sox2 binding during human neuroectodermal commitment. *Cell Death Differ.* **24**, 1121–1131 (2017).
66. Tan, Y., Xue, Y., Song, C. & Grunstein, M. Acetylated histone H3K56 interacts with Oct4 to promote mouse embryonic stem cell pluripotency. *Proc. Natl Acad. Sci. USA* **110**, 11493–11498 (2013).
67. Baumann, C., Zhang, X., Zhu, L., Fan, Y. & De La Fuente, R. Changes in chromatin accessibility landscape and histone H3 core acetylation during valproic acid-induced differentiation of embryonic stem cells. *Epigenet. Chromatin* **14**, 58 (2021).
68. Kang, J., Kang, Y. & Kim, A. Histone H3K4ac, as a marker of active transcription start sites and enhancers, plays roles in histone eviction and RNA transcription. *Biochim Biophys. Acta Gene Regul. Mech.* **1867**, 195021 (2024).
69. Li, D. et al. Chromatin accessibility dynamics during iPSC reprogramming. *Cell Stem Cell* **21**, 819–833.e816 (2017).
70. Cao, S. et al. Chromatin accessibility dynamics during chemical induction of Pluripotency. *Cell Stem Cell* **22**, 529–542.e525 (2018).
71. Kuang, J. et al. SS18 regulates pluripotent-somatic transition through phase separation. *Nat. Commun.* **12**, 4090 (2021).
72. Qin, Y. et al. Regeneration of the human segmentation clock in somitoids in vitro. *EMBO J.* **41**, e110928 (2022).
73. Huang, T. et al. Engineering mouse cell fate controller by rational design. *Nat. Commun.* **15**, 6200 (2024).
74. Zhang, G. et al. CPT1A induction following epigenetic perturbation promotes MAVS palmitoylation and activation to potentiate antitumor immunity. *Mol. Cell* **83**, 4370–4385.e4379 (2023).
75. Galle, E. et al. H3K18 lactylation marks tissue-specific active enhancers. *Genome Biol.* **23**, 207 (2022).
76. Zhang, D. et al. Metabolic regulation of gene expression by histone lactylation. *Nature* **574**, 575–580 (2019).

77. Chen, J. et al. Rational optimization of reprogramming culture conditions for the generation of induced pluripotent stem cells with ultra-high efficiency and fast kinetics. *Cell Res.* **21**, 884–894 (2011).
78. Kim, D., Paggi, J. M., Park, C., Bennett, C. & Salzberg, S. L. Graph-based genome alignment and genotyping with HISAT2 and HISAT-genotype. *Nat. Biotechnol.* **37**, 907–915 (2019).
79. Kovaka, S. et al. Transcriptome assembly from long-read RNA-seq alignments with StringTie2. *Genome Biol.* **20**, 278 (2019).
80. Dobin, A. et al. STAR: ultrafast universal RNA-seq aligner. *Bioinformatics* **29**, 15–21 (2013).
81. He, J. et al. Identifying transposable element expression dynamics and heterogeneity during development at the single-cell level with a processing pipeline scTE. *Nat. Commun.* **12**, 1456 (2021).
82. Love, M. I., Huber, W. & Anders, S. Moderated estimation of fold change and dispersion for RNA-seq data with DESeq2. *Genome Biol.* **15**, 550 (2014).
83. Korotkevich, G. et al. Fast Gene Set Enrichment Analysis. *bioRxiv* (Cold Spring Harbor Laboratory, 2016) https://doi.org/10.1101/060012.
84. Wu, T. et al. clusterProfiler 4.0: A universal enrichment tool for interpreting omics data. *Innovations* **2**, 100141 (2021).
85. Yu, G., Wang, L. G., Han, Y. & He, Q. Y. clusterProfiler: an R package for comparing biological themes among gene clusters. *OMICS* **16**, 284–287 (2012).
86. Langmead, B. & Salzberg, S. L. Fast gapped-read alignment with Bowtie 2. *Nat. Methods* **9**, 357–359 (2012).
87. Ramirez, F. et al. deepTools2: a next generation web server for deep-sequencing data analysis. *Nucleic Acids Res.* **44**, W160–W165 (2016).
88. Zhang, Y. et al. Model-based analysis of ChIP-Seq (MACS). *Genome Biol.* **9**, R137 (2008).
89. Quinlan, A. R. & Hall, I. M. BEDTools: a flexible suite of utilities for comparing genomic features. *Bioinformatics* **26**, 841–842 (2010).
90. Heinz, S. et al. Simple combinations of lineage-determining transcription factors prime cis-regulatory elements required for macrophage and B cell identities. *Mol. Cell* **38**, 576–589 (2010).
91. Robinson, J. T. et al. Integrative genomics viewer. *Nat. Biotechnol.* **29**, 24–26 (2011).
92. Jassal, B. et al. The reactome pathway knowledgebase. *Nucleic Acids Res.* **48**, D498–D503 (2020).

Acknowledgements

We thank Dr. Yu and Dr. Cao provided EpiSCs and suggestions in cell culture, and Dr. Liang provided technical support in proteomics. We also thank members of the Pei lab at Westlake University for their kind help, and the Mass Spectrometry & Metabolomics Platform, Flow Cytometry Platform, Microscopic Imaging Platform, and the General Equipment Core Facility in Westlake University for providing equipment and excellent service. This work was supported by the National Natural Science Foundation of China (92068201, 32300639, 32300672) and the Key R&D Program of Zhejiang (2024SSYS0031). This text was made clearer and more concise using ChatGPT and Grammarly.

Author contributions

D.P., Z.M., and X.H. designed the project; Z.M. performed the main experiments; X.H. performed the bioinformatic analysis; Z.M., Q.W., and W.L. performed the cell culture experiments; J.K., Y.Q. assisted in lipidomics, CUT&Tag analysis, and experiments designed; T.H., Z.L., Yu.F., P.L., and Yi.F. assisted in experiments including cell culture, Western Blot, RNA-seq, CUT&Tag seq, provided reagents and plasmids. Z.W., X.W., J.M., C.Z., and B.W. provided helpful suggestions and experimental materials. D.P. supervised and conceived the whole study, Z.M., X.H., and D.P. wrote the manuscript, D.P. approved the final version.

Competing interests

The authors declare no competing interests.

Additional information

Supplementary information The online version contains supplementary material available at https://doi.org/10.1038/s42003-024-06874-3.

Correspondence and requests for materials should be addressed to Duanqing Pei.

Peer review information *Communications Biology* thanks Leo Kurian and the other, anonymous, reviewer(s) for their contribution to the peer review of this work. Primary Handling Editors: Mo Li and Joao Valente. A peer review file is available.